Revealing non-covalent interactions in solids: NCI plots revisited

Alberto Otero-de-la-Roza,*[a] Erin R. Johnson,[a] and Julia Contreras-García[b]

Received Xth XXXXXXXXXX 20XX, Accepted Xth XXXXXXXXX 20XX
First published on the web Xth XXXXXXXXXX 200X
DOI: 10.1039/b000000x

In this article, the NCI method [Johnson *et al., J. Am. Chem. Soc.*, 2010, **132**, 6498] for plotting and analysis of non-covalent interactions (NCI) is extended to periodic (solid-state) electron densities and implemented in the CRITIC program. The new code uses self-consistent electron densities from a variety of electronic structure methods (pseudopotentials/plane-wave, FP-LAPW, local orbitals,...), and it can also build the promolecular density from the crystal geometry alone. As an example of the new code, intermolecular interactions in several molecular crystals are presented and analyzed. The connection with QTAIM studies is established and a reinterpretation of the NCI domains is given regarding the current knowledge of the field. The connection between NCI domains and intermolecular vibrations is made apparent, as well as the ability of the method to reveal the locality of bonding.

1 Introduction

A diverse collection of interactions, including electrostatics, hydrogen-bonding, dispersion, and Pauli repulsion, fall under the umbrella of non-covalent interactions[1–4]. This list has been expanded by the search for molecular aggregation patterns, called *synthons*, in the field of crystal engineering[5–7], and now includes halogen bonds[8,9], C–H$\cdots\pi$[10], C–H$\cdots$lone-pair[11], and lone-pair$\cdots\pi$[12] interactions.

The recently-developed NCI index[4,13,14] is capable of mapping real-space regions where non-covalent interactions are important and is based exclusively on the electron density and its gradient. The information provided by NCI plots is essentially qualitative (which molecular regions interact) or at best semi-quantitative (relating properties integrated within these regions with hydrogen-bond energies[14]). Solids usually present an even wider range of interactions than molecules[15] (in particular metallic and ionic interactions) and different interaction types are finely balanced to control the packing and stability of a crystal.

The objective of this work is to present the implementation of NCI for solid-state (periodic) densities using the second version of the CRITIC code[16]. This program can treat plane-wave, linearized augmented plane-wave, or local exponential basis sets, as opposed to the previous implementation which only considered molecular densities using Gaussian basis sets[13]. The NCI index relies exclusively on the electron density and its derivatives, so its implementation in solids also opens interesting new perspectives for the analysis of X-ray experimental densities[17,18,18,19].

A key conceptual problem in real-space visualization and characterization of non-covalent interactions is that of locality[20,21] because they can vary from close contacts, such as H-bonds, to highly-delocalized, long-range interactions, such as dispersion. Additionally, a problem with experimental (and occasionally theoretical[22]) densities is that noise and artifacts of the model density can complicate localization of the critical points and interatomic surfaces necessary for QTAIM analysis[18,21]. Through several representative examples, we show in this work that NCI plots avoid complex algorithms and numerical pitfalls, while offering valuable crystal bonding information.

2 The NCI method

The NCI method[4,13,14] relies on two scalar fields to map local bonding properties: the electron density (ρ) and the reduced-density gradient (RDG, s), defined as:

$$s = \frac{1}{2(3\pi^2)}\frac{|\nabla\rho|}{\rho^{4/3}}, \tag{1}$$

a quantity that is essential in the design of DFT functionals. The combination of s and ρ allows a rough partition of real space into bonding regions: high-s low-ρ corresponds to non-interacting density tails, low-s high-ρ to covalent bonds, and low-s low-ρ to non-covalent interactions.

[a] *Chemistry and Chemical Biology, School of Natural Sciences, University of California, Merced, 5200 North Lake Road, Merced, California 95343, USA; E-mail: aoterodelaroza@ucmerced.edu*
[b] *Laboratoire de Chimie Thèorique, Université Pierre et Marie Curie,75005 Paris, France*
‡ Additional footnotes to the title and authors can be included *e.g.* 'Present address:' or 'These authors contributed equally to this work' as above using the symbols: ‡, §, and ¶. Please place the appropriate symbol next to the author's name and include a `\footnotetext` entry in the the correct place in the list.

The second ingredient of the NCI index is the classification of interactions as attractive or repulsive according to the sign of the second density Hessian eigenvalue (λ_2). This distinguishes bonding interactions, where the electron density is locally accumulated with respect to the plane perpendicular to the bond path ($\lambda_2 < 0$) from the non-bonding interactions or steric clashes ($\lambda_2 > 0$). In QTAIM terms, the $\lambda_2 < 0$ NCI regions correspond to the loci near the intermolecular bond critical points (BCPs) while $\lambda_2 > 0$ are rings (RCPs, $\lambda_3 < 0$) and cages (CCPs, all λ positive).

In the practical, computational procedure an analytical or grid-based representation of the self-consistent electron density is obtained from a quantum-mechanical calculation or built from a superposition of atomic densities. A parallelepiped spanning the region of interest is chosen and a regular grid is built to encompass it. At each grid point, ρ and s are calculated by appropriate numerical or analytical differentiation and ρ is multiplied by the sign of λ_2. Plots of s versus $\mathrm{sign}(\lambda_2)\rho$ give the characteristic stiletto-heel shape[4,13,14]. The user must set two cutoff values in order to generate the three-dimensional NCI isosurface plot. The first cutoff is the reduced-gradient isovalue, s_{iso}. The value of $\mathrm{sign}(\lambda_2)\rho$ is color-mapped onto the s-isosurfaces with two density-cutoff values, ρ^-_{cut} and ρ^+_{cut}, used to set the color scale. The favored color scheme is a red-green-blue scale with red for ρ^+_{cut} (repulsive) and blue for ρ^-_{cut} (attractive)[13]. This is exemplified for the oxalic acid crystal in figure 1.

The structure of α-oxalic acid is composed of interacting layers of molecules strongly bound by hydrogen bonds[27]. The motif in these layers is the tetramer shown at the bottom of figure 1, that corresponds to the tetramolecular middle layer in the top picture. The electron density alone clearly distinguishes between the hydrogen bonds (the peak at $\mathrm{sign}(\lambda_2)\rho \approx -0.05$) and the rest of the intermolecular interactions, represented by the wide band around zero density. The three-dimensional plot identifies the bonding regions corresponding to each of these peaks. The hydrogen bonds appear as round, very localized, blue NCI domains, in the region where oxygen and hydrogen atoms interact. A complementary $\mathrm{sign}(\lambda_2)\rho \approx 0.05$ incipient peak appears as a red rim on the hydrogen bond domains, a feature that has been analyzed in a previous work[14].

In addition to hydrogen bonds, NCI analysis reveals more subtle interactions that would have been missed from a simple analysis of distances[28]. The peaks in the negative $\mathrm{sign}(\lambda_2)\rho$ region correspond to contacts between the oxygen lone pairs and the positively-charged carboxylic carbon of the molecule behind. These weaker interactions are represented in green and correspond to the central region of the (s,ρ) plot. The localized, high-density NCI regions for hydrogen-bonds indicate a relatively strong, highly-directional, intermolecular interaction while the weak interactions extend over large regions

Fig. 1 The α phase of oxalic acid[23] (space group Pcab, $Z = 4$) at the equilibrium structure found using the B86b-XDM method[24,25] and the Quantum ESPRESSO code[26]. The crystal structure (top), the (s,ρ) diagram (middle) and the computed NCI regions (bottom) are shown. In the (s,ρ) representation, the RDG isovalue used is represented by a dotted line, and the color scale used by the thick continuous line. The blue arrow points to the peak corresponding to the global minimum of the electron density in the crystal.

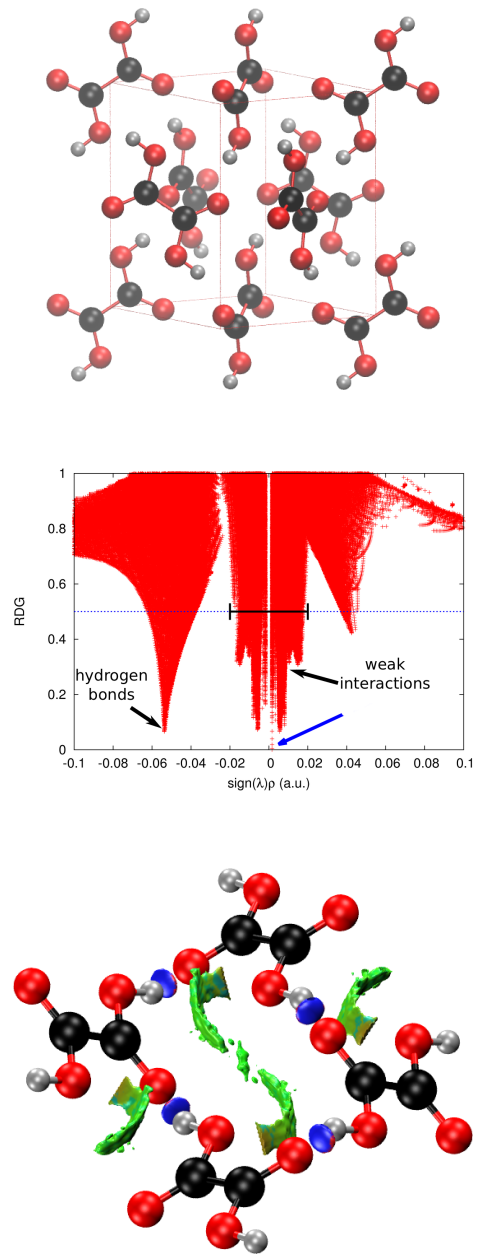

of intermolecular contacts. This information is useful when assessing the environment of a particular molecule in a host crystal.

The negative $\mathrm{sign}(\lambda_2)\rho$ region corresponds to QTAIM BCPs (associated with $s = 0$ points located inside the region) while the positive represents rings and cages. Contrary to molecules, where rings and particularly cages are relatively rare, the compact nature of real space in periodic solids imposes the presence of at least three rings and one cage because of the translation symmetry of the crystal[29]. Thus, peaks at positive density (signified by an arrow in figure 1) must always be present and represent the global minimum of the electron density in the crystal. Additionally, in high symmetry crystals NCI peaks (BCPs) associated with the fixed Wyckoff positions must appear. Molecular crystals have a high packing ratio so many intermolecular interactions appear around $\rho \leq 0.02$ a.u. that are clearly distinguished from more energetic contacts like hydrogen bonds. The interpretation of these domains is still a subject of debate (see section 4) but it is heartening that they systematically correspond to intuitive chemical interactions as happens in the case of α-oxalic acid.

3 Implementation of NCI in solids

We have implemented the NCI visualization method in the second version of the CRITIC code[16], which can use density information from Quantum ESPRESSO[26], abinit[30,31], VASP[32,33], WIEN2k[34–36], elk[37] or pi7[38] as input. In addition, CRITIC reads density cubes in gaussian[39] and XCrysden[40] formats, so any program not directly supported can be interfaced with CRITIC2 via (relatively sparse) density grids.

It is possible to restrict the number of grid points in a variety of convenient ways. In particular, in a PSPW code the density is represented as a uniform grid of ρ values spanning the periodic cell, which can be transformed to the corresponding reciprocal-space values ($\rho_{\boldsymbol{G}}$) using an efficient three-dimensional Fast Fourier Transform (FFT). This possibility is useful in the computation of the density derivatives that are required to build s and λ_2 because of the simple relationship between the density reciprocal-space coefficients and those of its derivatives. The coefficients of the density gradient and Hessian are transformed back into real-space, and then used to calculate the reduced density gradient and the Hessian eigenvalues. FFT is typically much more efficient than the simple loop over grid points, but the resulting grid necessarily extends over the complete unit cell and the density of the grid may be too low for an adequate representation. To overcome this limitation, a three-dimensional spline interpolation scheme[30,31] is used to calculate grids denser and in localized regions of space. The use of very dense grids at DFT level is commonplace in the analysis of PSPW results in QTAIM[41–43] and in this work it is avoided by using three-dimensional interpolation.

In order to assess the validity of the NCI plots obtained with interpolated PSPW densities, figure 2 compares NCI plots obtained from an all-electron full-potential LAPW calculation with the PSPW results for the poly-NPF_2 phosphazene. Polyphosphazenes are the largest class of inorganic polymers, with high fundamental and technological relevance[45]. Poly-NPF_2 is the simplest member in the family, and the only for which the crystal structure is partially known[44]. In figure 2, the interaction regions of poly-NPF_2 are shown. The PSPW domains are for practical purposes indistinguishable to those obtained using the all-electron method, while the generation of the grid scalar fields for the latter is approximately 30 times slower (of course, the electronic relaxation is also faster in PSPW than in LAPW). The total wall time to generate the NCI plot for poly-NPF_2 is less than a minute (8 processors desktop PC, 3.4 GHz) in the PSPW approach. The plots show a very weak and localized fluorine-fluorine interaction, similar to stronger halogen bonds[9], and an only slightly stronger, electrostatic interaction between fluorine and the N-P bond in the neighboring chain, which explains the difficulty in the crystallization of these polymers.

Because of the pseudopotentials, PSPW calculations only work with valence densities, which are smoother but also unphysical in the core regions. It is possible to reconstruct the all-electron density using the (frozen) core orbitals[47]. However, NCI plots are interesting only in valence regions, and their interpretation is qualitative, so we take the simple approach of adding a core density that accounts for the missing electrons. This procedure is similar to the construction of the promolecular densities and, in the practical implementation, the two tasks are bundled together. Atomic radial density grids from spherical atomic DFT calculations are used for all atoms in the periodic table. These distance interpolation tables contain the density contribution of all the atomic orbitals in the neutral configuration of the atom. If the promolecular density is needed, it is computed by summing over all orbitals. If only the core density is required, then the sum extends only up to the given number of electrons. This scheme retains the simplicity characteristic of the molecular NCI code[13].

Figure 3 shows the NCI plot of the cyanamide crystal[46] using self-consistent and promolecular densities at the calculated equilibrium structure. As noted previously[4,48], the qualitative features are similar, but electronic relaxation of the density tends to draw electrons from intermolecular regions. Consequently, self-consistent densities tend to displace intermolecular interactions to smaller values of ρ and give smaller surfaces, as shown in the plot. The qualitative features, however, are the same, and the intra-dimer hydrogen bonds and the inter-dimer dipole-dipole attraction are shown clearly in both cases.

Fig. 2 The phosphazene polymer poly-NPF_2, calculated at the experimental geometry[44] (left). The NCI plots were obtained using the PSPW approach (abinit code[30,31], middle) and the FPLAPW method (WIEN2k[34–36], right).

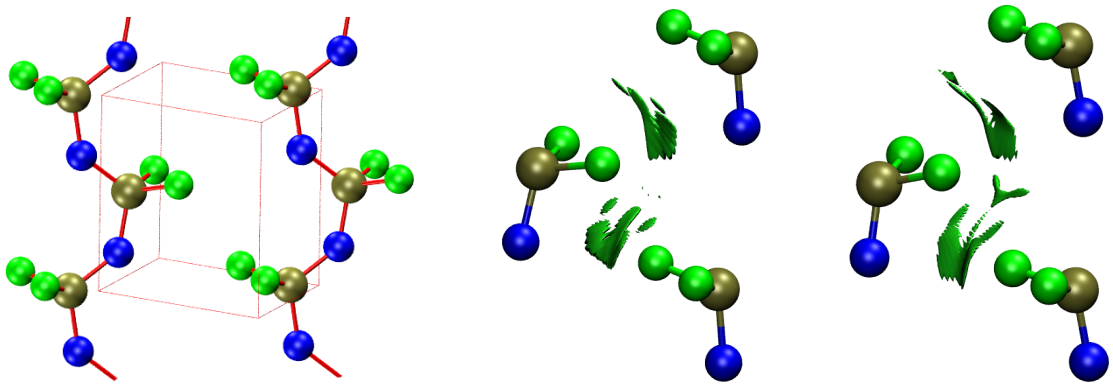

Fig. 3 NCI plots for the cyanamide crystal[46] (space group Pbca, $Z = 8$) at the equilibrium geometry calculated using B86B-XDM. We represent the crystal cell (top left), the RDG *vs.* ρ plot (top right), and the NCI domains (below) for a pair of dimers using the self-consistent density calculated with the PSPW approach (Quantum ESPRESSO, left) and the promolecular density (PBE, right).

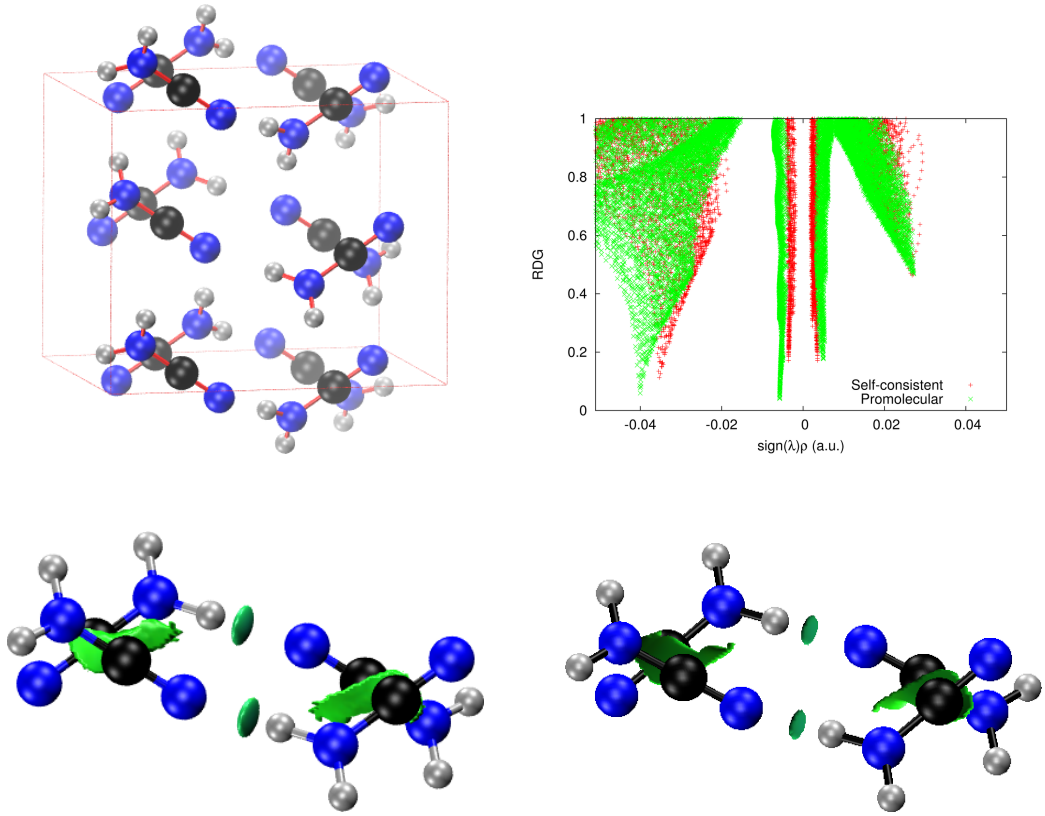

An important function of the new code is convenient visualization of the NCI regions. The representation of the whole unit cell is seldom informative because the interaction regions are usually straddled across the cell boundary. Also, entire molecules are frequently not contained in the interior of the cell for the conventional origin choice. To successfully present the NCI domains, several interacting molecules must be isolated and only the NCI regions associated with those molecules must be represented. This is achieved by suitably shrinking the representation grids and by considering only the grid nodes for which i) more than a fraction $f_{\max}$ (≈ 0.95) of the promolecular density comes from the selected fragments and ii) the contribution of each fragment is less than a certain fraction $f_{\min}$ (≈ 0.75) of the total density. All figures in this article exemplify the use of this technique.

4 Interpretation of the NCI domains

Thanks to its simplicity, NCIplot has enjoyed a good deal of popularity in its short life. In previous articles[4,13,14], the NCI domains were identified with non-bonded attractive or repulsive interactions based on systematic observations and chemical intuition. NCI regions enclose interstitial critical points, so they provide a faithful representation of the atomic bonding network, as defined in QTAIM[49–51], the leading theory in the analysis of solid-state chemical bonding[21]. Because QTAIM relies exclusively on the electron density, it is especially useful in the field of experimental X-ray densities. NCI plots in solids, however, present several advantages as an alternative over traditional QTAIM critical point maps: i) the numerical and algorithmic problems in locating exactly the position of the critical points are avoided, ii) the transition from bonding to non-bonding situations is gradual instead of catastrophic and iii) the NCI regions can provide information about the extent of the interaction in real space. Indeed, the usefulness of NCI in solid-state applications will soon be tested on experimental densities.

Figure 4 shows how the NCI index behaves in simple crystals with different basic bonding patterns. The plots are consistent with the known real-space features of the electron density. In a metal, the density is almost flat throughout the interstitial region[15] and the bonding network is labile[52]. This translates into spherical s-isosurfaces at low s and ρ values. Similarly, fcc neon domains also appear at a low density value, but in this case contacts are localized between atoms instead of smeared over the crystal voids. Even though the (s,ρ) peaks are similar for the metal and the noble-gas crystal, localization of the domains in real space allows one to be differentiated from the other. Comparison of fcc neon to the ionic NaF crystal is also interesting because they are formally isoelectronic, so they represent a simple test of how NCI domains behave when the crystal geometry is similar but the chemical behavior of atoms is widely different. In NaF, there is a charge transfer from Na to F that causes anion-anion contacts appear, a feature that has been reported in previous QTAIM studies of ionic solids[29,53–56]. The strongest interaction, in terms of electron density at the NCI domain, is still the cation-anion contact. NCI domains are more abundant and larger in NaF than in Ne, which is consistent with the former being much more strongly bound thanks to point-charge-like electrostatic interactions.

The NCIplot technique reveals the bonding regions and interaction strengths of hydrogen-bonds as shown in figure 5 for the case of the urea crystal[57,58]. There are two different kinds of hydrogen bonds in urea: a stronger one represented as a blue round domain ($d(\mathrm{O...H}) = 2.026$Å) and the weaker hydrogen bond represented as a round green domain ($d(\mathrm{O...H}) = 2.335$Å). It is interesting to note that application of Espinosa's relation[59] between the dissociation energy of a hydrogen bond and $d(\mathrm{O...H})$ yields 4.22 and 1.41 kcal/mol, that combine to give a crystal binding energy of 11.26 kcal/mol. This value is much smaller than the experimental sublimation enthalpy (around 21.5 kcal/mol[27]) so, even though hydrogen bonds determine molecular orientations in the crystal, weaker interactions still account for almost half of the experimental binding energy of the urea crystal. Figure 5 reveals one of these weaker interactions: the dipole-dipole attraction of N–H in neighboring urea molecules. This observation evidences the perils involved in representing the crystal as a dimer or trimer extruded from the experimental molecular packing, backing previous statements about the appearance of QTAIM bond paths being inextricably linked to the chemical environment[21].

The meaning of intermolecular BCPs corresponding to interactions weaker than hydrogen bonds is less clear. A simple example is the case of endohedral bonds in the inclusion complex He@adamantane[28,60,61]. The dissociation of He@adamantane is exothermic, with a dissociation energy of -154 kcal/mol[60]. At the equilibrium geometry, the adamantane cage is stretched with respect to its geometry when empty. The intuitive explanation is that the steric repulsion between the He atom and the adamantane cage causes the stretching and the energy raise. This explanation is denied within the QTAIM energy partition[61] where at the equilibrium geometry of the complex, the He atom actually attracts the adamantane cage, and it is the lengthening of the C–C bonds that is responsible for the destabilization. Within orthodox QTAIM, there is no *a priori* explanation for the stretching of these bonds. The interpretation of endohedral contacts in terms of closed-shell repulsion requires an energy partition that contains this term[20,62]. Similar occurrences of this interpretative problem appear, for instance, in anion-anion contacts[29,53–55], halogen-halogen bonding[56,63] and dihydrogen bonding (see below).

Whether weaker intermolecular NCI contacts are read as at-

Fig. 4 NCI plots for ionic (NaF, left), metallic (bcc sodium, middle) and noble gas (fcc Ne, right) solids at their experimental geometries, computed using FPLAPW as implemented in the elk program[37].

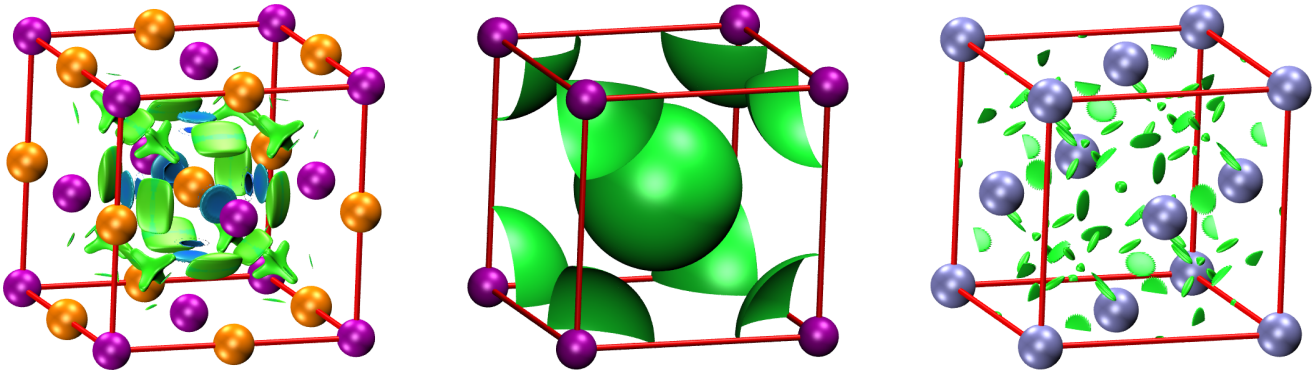

Fig. 5 NCI plots for urea at the B86b-XDM equilibrium geometry calculated using Quantum ESPRESSO. The unit cell is shown on the left and the NCI plots for three interacting molecules on the right.

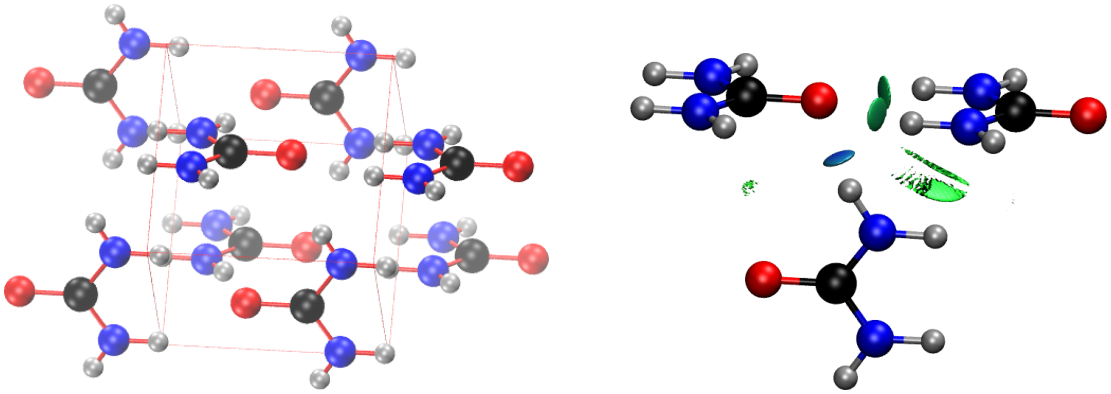

Fig. 6 NCI regions of carbon dioxide (Quantum ESPRESSO, equilibrium geometry, B86b-XDM). The arrows represent the three degenerate highest-frequency intermolecular phonons at the Γ point and correspond to rotations of the CO_2 molecules. Each of the three modes is represented in a different color.

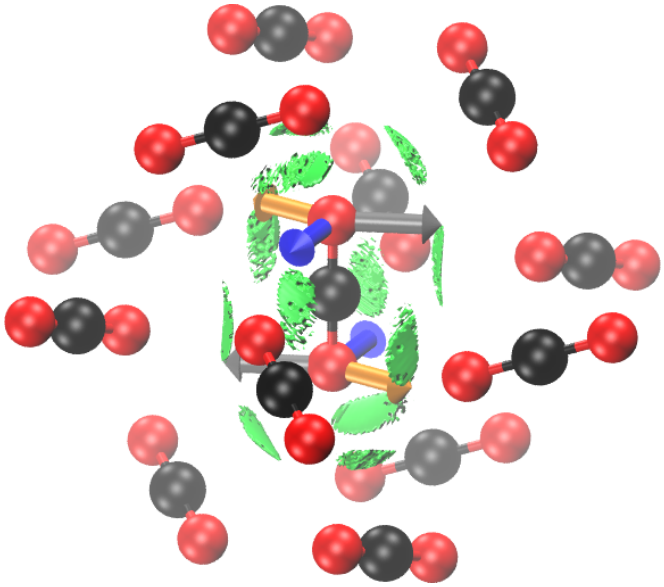

tractions or repulsions, it is clear that the intermolecular density build-up they represent marks an atomic interaction. The accumulation of density affects the forces via the Hellmann-Feynman theorem, as first studied by Berlin in his seminal work[64]. This effect can be readily evidenced by matching the position of NCI regions and the atomic movements along stiff intermolecular vibrational modes. For instance, figure 6 shows the $\lambda_2 < 0$ regions of carbon dioxide, together with the highest frequency intermolecular vibrational modes at Γ ($\nu_{18} = \nu_{19} = \nu_{20} = 120\ \mathrm{cm}^{-1}$). The NCI regions appear associated to the regions where molecules come into contact under these vibrations (that correspond to molecular rotations in the crystal matrix). The interpretation in terms of closed-shell repulsions is straightforward: at the equilibrium geometry, Pauli repulsion balances the rest of attractive interactions (electrostatic, dispersion,...) and the total atomic forces are zero. Disregarding intramolecular modes, that are effectively decoupled from intermolecular ones in this case, the least favorable direction in which atoms can move corresponds exactly to the directions of maximum density overlap, hence the result in figure 6. The relation between Pauli repulsion and density build-up in the intermolecular zone is also the basis of Bondi's definition of van der Waals radii[65].

A fundamental problem in crystal packing is understanding the role of weak hydrogen-hydrogen contacts, a problem similar to endohedral bonds, and still an open question[20,21,28,62,66–72]. The H–H BCPs were first interpreted by

Fig. 7 NCI interaction regions for benzene, calculated at the equilibrium B86b-XDM structure.

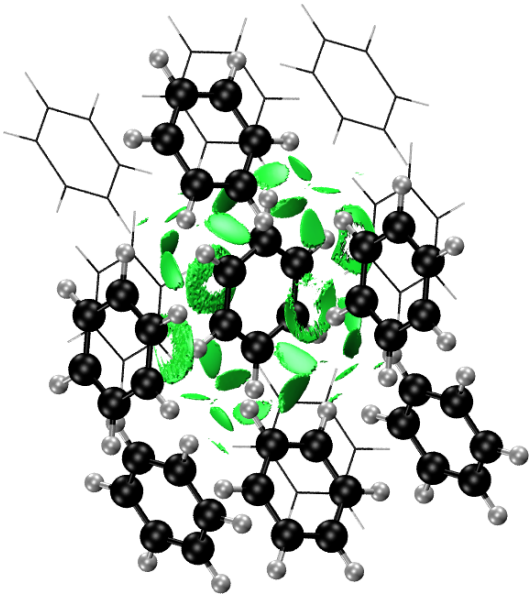

Cioslowski and Mixon in kekulene[66] and ortho-substituted biphenyls[67] and assigned to "non-bonded repulsive contacts", a view supported by later studies with different energy partitions[20,62,71]. QTAIM atomic energies, on the other hand, predict a stabilization caused by H–H contacts of up to 10 kcal/mol in the general case of polybenzenoid molecules[70]. It is clear that the weakness of dihydrogen interactions and the arbitrariness in the choice of energy partition precludes determining whether these interactions are favorable or unfavorable to molecular packing and how much they contribute to the total binding energy of a crystal.

Hydrogen-hydrogen contacts are revealed by NCI plots, as shown in figure 7 for benzene. As evidenced by PIXEL calcualtions[20,73,74], benzene packing arises from long-range dispersion and electrostatic interactions and the preference of benzene for the *Pbca* arrangement instead of, for instance, the $P2_1/c$ structure (as is the case of heavier acenes) is still poorly understood. The main reason is the minute energy difference between polymorphs[20]. In the *Pbca* structure, each benzene molecule is surrounded by 12 molecules in a distorted fcc arrangament. NCI reveals the local intermolecular contact regions: CH$\ldots\pi$ (the rings parallel to the central benzene molecule), C$\cdots$HC and dihydrogen. The latter appear only between hydrogens that are at a distance similar to the sum of the van der Waals radius of H (1.2Å). It is interesting to note that dihydrogen and C$\cdots$CH contacts are local: the NCI domains are localized in extent, resembling stronger hydrogen bonds but at much lower densities. In contrast, the CH$\cdots\pi$ interaction occurs between hydrogen and the whole neighboring

benzene ring. The shape of these NCI domains is essentially different from those corresponding to hydrogen bonds. In the latter, the directionality is characterized by the small, round shape of the regions and the strength by the relatively large accumulation of electron density. Weaker interactions such as the ones found in benzene give rise to interaction regions, rather than localized NCI domains, and presenting a relatively low elecron density. NCI plots map regions instead of atom-atom contacts, a point that is usually raised about QTAIM bonding networks[20,21].

The thymine crystal (figure 8) is a further example of how NCI differentiates between localized atom-atom contacts corresponding to strong directional attractions and weakly-interacting molecular regions. The crystal arrangement consists of layers of hydrogen-bonded thymine molecules. These layers are stacked in parallel so that the electrostatic attraction between dipoles in neighboring layers is maximized. In the figure, the strong intra-layer hydrogen bonds appear as round blue domains in the case of close H...O contacts or as green round domains for weaker hydrogen bonds. The inter-layer picture of bonding, however, presents extensive regions of intermolecular interaction, with an overall low density, consistent with a more delocalized bonding.

To conclude this section, we consider the interpretation of the $\lambda_2 > 0$ domains, corresponding to rings and cages in QTAIM. In previous NCI studies these have been associated to destabilizing steric clashes[4,13,14] because they appear at the center of rings or voids in sterically constrained molecules. The appearance of these domains in solids, however, is forced by translational symmetry, even if the cell is infinitely stretched. Considering the above discussion, we can argue that the steric clashes, in the sense of closed-shell repulsions balanced by other attractive forces at equilibrium, actually correspond to $\lambda_2 < 0$ and that positive λ_2 regions are found whenever there is a void in the crystal. A possible interpretation of the effect on the binding energy of these voids can be made in the sense of Kitaigorodskii's ideas[75,76]: molecules tend to adapt their shape to achieve the closest packing possible, in a sort of key-and-lock mechanism. In this view, voids are destabilizing with respect to any other crystal packing not having them because they are a waste of molecular space. The $\lambda_2 > 0$ regions can be thought as (destabilizing) empty space, and also a place where the introduction of substituents or new molecular species is possible. In any case, care is recommended when interpreting the sign of λ_2 in very weak interactions, because in these cases the sign might depend on the method of calculation.

Fig. 8 The thymine crystal at the equilibrium geometry (B86b-XDM) is shown on the left. The molecular packing is made of stacked layers of hydrogen-bonded molecules. The inter-layer (middle) and intra-layer (bottom) NCI regions are shown.

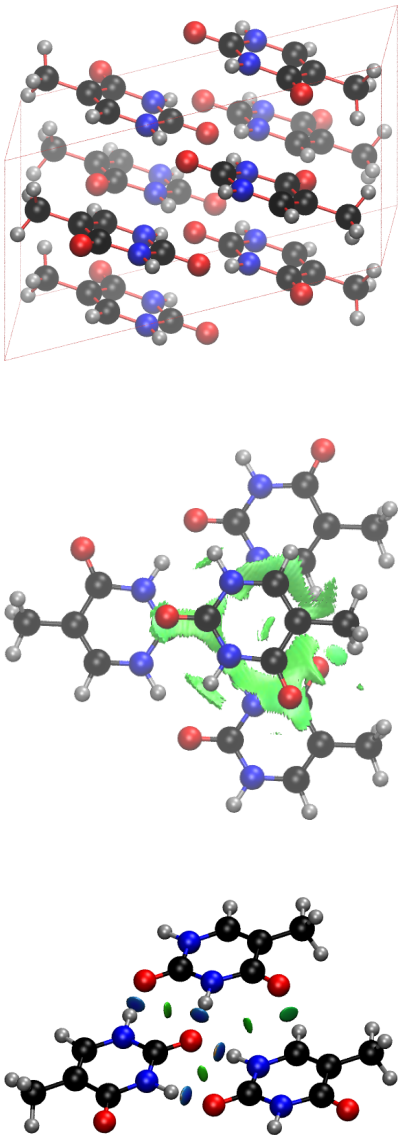

5 Conclusions

In this article, we have presented the implementation of the NCI method for the analysis of densities under periodic

boundary conditions in the CRITIC code, which will be available to the public under free license in the near future. The NCI method maps non covalent interactions (NCI) arising between molecular fragments into real space using solely the electron density as input. In the simplest case, the density is built as a sum of atomic densities and only the atomic arrangement is required, an option that is interesting in very large systems.

The new code provides an abstraction layer over different computational techniques, basis-set expressions and file formats used commonly in the solid-state community. In the particular case of the pseudopotentials/plane-waves method, densities are expressed on a regular grid, and we have described a flexible and efficient method to calculate the NCI domains. In addition, the ability to read densities on a three-dimensional grid enables our program to interface with virtually any solid-state code.

The interpretation of NCI regions has been placed into the context of the literature by connection with QTAIM critical points. Two possible meanings of the $\lambda_2 < 0$ domains are possible i) the traditional QTAIM view where these regions are always attractive, and ii) an interpretation where the density build-up represented by the NCI domains corresponds to intermolecular Pauli repulsions that are balanced by other attractive forces (electrostatic, dispersion,...). While the energy partition in the former is less arbitrary, the latter allows an interpretation of crystal packing in agreement with previous chemical thinking. In addition, it has been shown that NCI domains correspond to regions marking the stiffest intermolecular vibrational modes in the crystal.

We have shown that the atom-to-atom picture of QTAIM bonding networks is replaced in NCI by a real-space mapping whose properties depend on the nature of the interaction. While hydrogen-bonds are represented by small round domains with a relatively high density, weaker and less directional interactions are smeared over wide regions of real-space. NCI domains, therefore, are able to recover the locality and directionality of bonding. Finally, the $\lambda_2 > 0$ regions are reinterpreted as voids in the crystal structure that represent a destabilization in the sense of decreased molecular packing.

6 Acknowledgements

AOR and JCG thank the Spanish Malta/Consolider initiative (no. CSD2007-00045). JCG thanks the Spanish Ministry of Education for a postdoctoral grant.

References

1 A. Gavezzotti, *Theoretical aspects and computer modeling of the molecular solid state*, J. Wiley, 1997.
2 C. Gray and K. Gubbins, *Theory of molecular fluids*, Clarendon Press Oxford, 1984.
3 A. Stone and A. Stone, *The theory of intermolecular forces*, Clarendon Press Oxford, 1996.
4 E. Johnson, S. Keinan, P. Mori-Sánchez, J. Contreras-García, A. Cohen and W. Yang, *J. Am. Chem. Soc.*, 2010, **132**, 6498–6506.
5 F. Allen, *Acta Cryst. B*, 2002, **58**, 380–388.
6 G. Desiraju, *Angew. Chem. Intl. Ed. Engl.*, 1995, **34**, 2311–2327.
7 G. Desiraju, *Angew. Chem. Intl. Ed.*, 2007, **46**, 8342–8356.
8 P. Metrangolo and G. Resnati, *Chem. Eur. J.*, 2001, **7**, 2511–2519.
9 A. Gavezzotti, *Mol. Phys.*, 2008, **106**, 1473–1485.
10 G. Desiraju, *Acc. Chem. Res.*, 1996, **29**, 441–449.
11 J. Dunitz and W. Schweizer, *Chem. Eur. J.*, 2006, **12**, 6804–6815.
12 J. Zukerman-Schpector, A. Otero-de-la Roza, V. Luaña and E. R. T. Tiekink, *Chem. Commun.*, 2011, **47**, 7608–7610.
13 J. Contreras-García, E. Johnson, S. Keinan, R. Chaudret, J. Piquemal, D. Beratan and W. Yang, *J. Chem. Theory Comput.*, 2011, **7**, 625–632.
14 J. Contreras-García, W. Yang and E. Johnson, *J. Phys. Chem. A*, 2011, **115**, 12983–12990.
15 P. Mori-Sánchez, A. Pendás and V. Luaña, *J. Am. Chem. Soc.*, 2002, **124**, 14721–14723.
16 A. Otero-de-la Roza, M. Blanco, A. Pendás and V. Luaña, *Comput. Phys. Commun.*, 2009, **180**, 157–166.
17 P. Coppens, *X-ray charge densities and chemical bonding*, Oxford University Press, USA, 1997.
18 P. Coppens, *Angew. Chem. Intl. Ed.*, 2005, **44**, 6810–6811.
19 T. Koritsanszky and P. Coppens, *Chem. Rev.*, 2001, **101**, 1583–1628.
20 J. Dunitz and A. Gavezzotti, *Angew. Chem. Intl. Ed.*, 2005, **44**, 1766–1787.
21 C. Gatti, *Z. Kristallogr.*, 2005, **220**, 399–457.
22 A. Otero-de-la Roza and V. Luaña, *J. Chem. Theory Comput.*, 2010, 3761–3779.
23 J. Derissen and P. Smith, *Acta Cryst. B*, 1974, **30**, 2240–2242.
24 A. Becke, *J. Chem. Phys.*, 1986, **85**, 7184.
25 A. Otero-de-la Roza and E. R. Johnson, 2012, J. Chem. Phys., (accepted).
26 P. Giannozzi, S. Baroni, N. Bonini, M. Calandra, R. Car, C. Cavazzoni, D. Ceresoli, G. Chiarotti, M. Cococcioni, I. Dabo *et al.*, *J. Phys.: Condens. Matter*, 2009, **21**, 395502.
27 W. Acree Jr and J. Chickos, *J. Phys. Chem. Ref. Data*, 2010, **39**, 043101.
28 A. Pendás, E. Francisco, M. Blanco and C. Gatti, *Chem. Eur. J.*, 2007, **13**, 9362–9371.
29 A. Pendás, A. Costales and V. Luaña, *Phys. Rev. B*, 1997, **55**, 4275.
30 X. Gonze, J. Beuken, R. Caracas, F. Detraux, M. Fuchs, G. Rignanese, L. Sindic, M. Verstraete, G. Zerah, F. Jollet *et al.*, *Comput. Mater. Sci.*, 2002, **25**, 478–492.
31 X. Gonze, *Z. Kristallogr.*, 2005, **220**, 558–562.
32 G. Kresse and J. Furthmüller, *Comput. Mat. Sci.*, 1996, **6**, 15.
33 G. Kresse and J. Furthmüller, *Phys. Rev. B*, 1996, **54**, 11169.
34 K. Schwarz, P. Blaha and G. K. H. Madsen, *Comput. Phys. Commun.*, 2002, **147**, 71–76.
35 K. Schwarz and P. Blaha, *Comput. Mater. Sci.*, 2003, **28**, 259–273.
36 K. Schwarz, P. Blaha and G. K. H. Madsen, *Comput. Phys. Commun.*, 2002, **147**, 71–76.
37 K. Dewhurst, S. Sharma *et al.*, *The Elk FP-LAPW code*, `http://elk.sourceforge.net/`.
38 V. Luaña, A. Martín Pendás, J. Recio, E. Francisco and M. Bermejo, *Comp. Phys. Commun.*, 1993, **77**, 107–134.
39 M. J. Frisch, G. W. Trucks, H. B. Schlegel, G. E. Scuseria, M. A. Robb, J. R. Cheeseman, G. Scalmani, V. Barone, B. Mennucci, G. A. Petersson, H. Nakatsuji, M. Caricato, X. Li, H. P. Hratchian, A. F. Izmaylov, J. Bloino, G. Zheng, J. L. Sonnenberg, M. Hada, M. Ehara, K. Toyota,

R. Fukuda, J. Hasegawa, M. Ishida, T. Nakajima, Y. Honda, O. Kitao, H. Nakai, T. Vreven, J. A. Montgomery, Jr., J. E. Peralta, F. Ogliaro, M. Bearpark, J. J. Heyd, E. Brothers, K. N. Kudin, V. N. Staroverov, R. Kobayashi, J. Normand, K. Raghavachari, A. Rendell, J. C. Burant, S. S. Iyengar, J. Tomasi, M. Cossi, N. Rega, J. M. Millam, M. Klene, J. E. Knox, J. B. Cross, V. Bakken, C. Adamo, J. Jaramillo, R. Gomperts, R. E. Stratmann, O. Yazyev, A. J. Austin, R. Cammi, C. Pomelli, J. W. Ochterski, R. L. Martin, K. Morokuma, V. G. Zakrzewski, G. A. Voth, P. Salvador, J. J. Dannenberg, S. Dapprich, A. D. Daniels, . Farkas, J. B. Foresman, J. V. Ortiz, J. Cioslowski and D. J. Fox, *Gaussian 09 Revision A.1*, Gaussian Inc. Wallingford CT 2009.

40 A. Kokalj, *Journal of Molecular Graphics and Modelling*, 1999, **17**, 176–179.

41 G. Henkelman, A. Arnaldsson and H. Jónsson, *Comput. Mater. Sci.*, 2006, **36**, 354–360.

42 E. Sanville, S. Kenny, R. Smith and G. Henkelman, *J. Comp. Chem.*, 2007, **28**, 899–908.

43 W. Tang, E. Sanville and G. Henkelman, *J. Phys.: Condens. Matter*, 2009, **21**, 084204.

44 H. R. Allcock, R. L. Kugel and E. G. Stroh, *Inorg. Chem.*, 1972, **11**, 1120–1123.

45 V. Luaña, A. Pendás, A. Costales, G. Carriedo and F. García-Alonso, *J. Phys. Chem. A*, 2001, **105**, 5280–5291.

46 L. Denner, P. Luger and J. Buschmann, *Acta Cryst. C*, 1988, **44**, 1979–1981.

47 E. Aubert, S. Lebegue, M. Marsman, T. T. T. Bui, C. Jelsch, S. Dahaoui, E. Espinosa and J. G. Ángyán, *J. Phys. Chem. A*, 2011, **115**, 14484–14494.

48 M. Spackman and E. Maslen, *J. Phys. Chem.*, 1986, **90**, 2020–2027.

49 R. F. W. Bader, *Atoms in Molecules.A Quantum Theory*, Oxford University Press, Oxford, 1990.

50 R. F. W. Bader, *Chem. Rev.*, 1991, **91**, 893–928.

51 *Topology and properties of the electron density in solids*, ed. R. Boyd and C. Matta, Wiley-VCH, Weinheim, Germany, 2007.

52 V. Luaña, P. Mori-Sánchez, A. Costales, M. A. Blanco and A. Pendás, *J. Chem. Phys.*, 2003, **119**, 6341.

53 Y. Abramov, *J. Phys. Chem. A*, 1997, **101**, 5725–5728.

54 A. Pendás, A. Costales and V. Luaña, *J. Phys. Chem. B*, 1998, **102**, 6937–6948.

55 R. Bader, *J. Phys. Chem. A*, 1998, **102**, 7314–7323.

56 F. Awwadi, R. Willett, K. Peterson and B. Twamley, *Chem. Eur. J.*, 2006, **12**, 8952–8960.

57 D. Jayatilaka and D. Grimwood, *Acta Cryst. A*, 2004, **60**, 111–119.

58 C. Gatti, V. R. Saunders and C. Roetti, *J. Chem. Phys.*, 1994, **101**, 10686–10696.

59 E. Espinosa, E. Molins and C. Lecomte, *Chem. Phys. Lett.*, 1998, **285**, 170–173.

60 A. Haaland, D. Shorokhov and N. Tverdova, *Chem. Eur. J.*, 2004, **10**, 4416–4421.

61 R. Bader and D. Fang, *J. Chem. Theory Comput.*, 2005, **1**, 403–414.

62 J. Poater, M. Sola and F. Bickelhaupt, *Chem. Eur. J.*, 2006, **12**, 2889–2895.

63 V. Tsirelson, P. Zhou, T. Tang and R. Bader, *Acta Cryst. A*, 1995, **51**, 143–153.

64 T. Berlin, *J. Chem. Phys.*, 1951, **19**, 208–213.

65 A. Bondi, *J. Phys. Chem.*, 1964, **68**, 441–451.

66 J. Cioslowski, S. Mixon and W. Edwards, *J. Am. Chem. Soc.*, 1991, **113**, 1083–1085.

67 J. Cioslowski and S. Mixon, *J. Am. Chem. Soc.*, 1992, **114**, 4382–4387.

68 G. Desiraju, *Acc. Chem. Res.*, 2002, **35**, 565–573.

69 K. Robertson, O. Knop and T. Cameron, *Can. J. Chem.*, 2003, **81**, 727–743.

70 C. Matta, J. Hernández-Trujillo, T. Tang and R. Bader, *Chem. Eur. J.*, 2003, **9**, 1940–1951.

71 S. Grimme, C. Mück-Lichtenfeld, G. Erker, G. Kehr, H. Wang, H. Beckers and H. Willner, *Angew. Chem. Intl. Ed.*, 2009, **48**, 2592–2595.

72 R. F. W. Bader, *J. Phys. Chem. A*, 2009, **113**, 10391–10396.

73 A. Gavezzotti, *J. Phys. Chem. B*, 2002, **106**, 4145–4154.

74 A. Gavezzotti, *J. Phys. Chem. B*, 2003, **107**, 2344–2353.

75 A. I. Kitaigorodskii, *Organic Chemical Crystallography*, Consultants Bureau, New York, 1961.

76 A. I. Kitaigorodskii, *Molecular crystals and molecules*, Academic Press, New York, 1973.